Supplementary Information

Deep learning enables fast, gentle STED microscopy

Vahid Ebrahimi[1], Till Stephan[2,3], Jiah Kim[4], Pablo Carravilla[5,6], Christian Eggeling[5,6,7,8], Stefan Jakobs[2,3,9], Kyu Young Han[1,*]

[1]CREOL, The College of Optics and Photonics, University of Central Florida, Orlando, FL, USA

[2]Department of NanoBiophotonics, Max Planck Institute for Multidisciplinary Sciences, Göttingen, Germany

[3]Department of Neurology, University Medical Center Göttingen, Göttingen, Germany

[4]Department of Cell and Developmental Biology, University of Illinois at Urbana-Champaign, Urbana, IL, USA

[5]Leibniz Institute of Photonic Technology e.V., Jena, Germany, member of the Leibniz Centre for Photonics in Infection Research (LPI), Jena, Germany

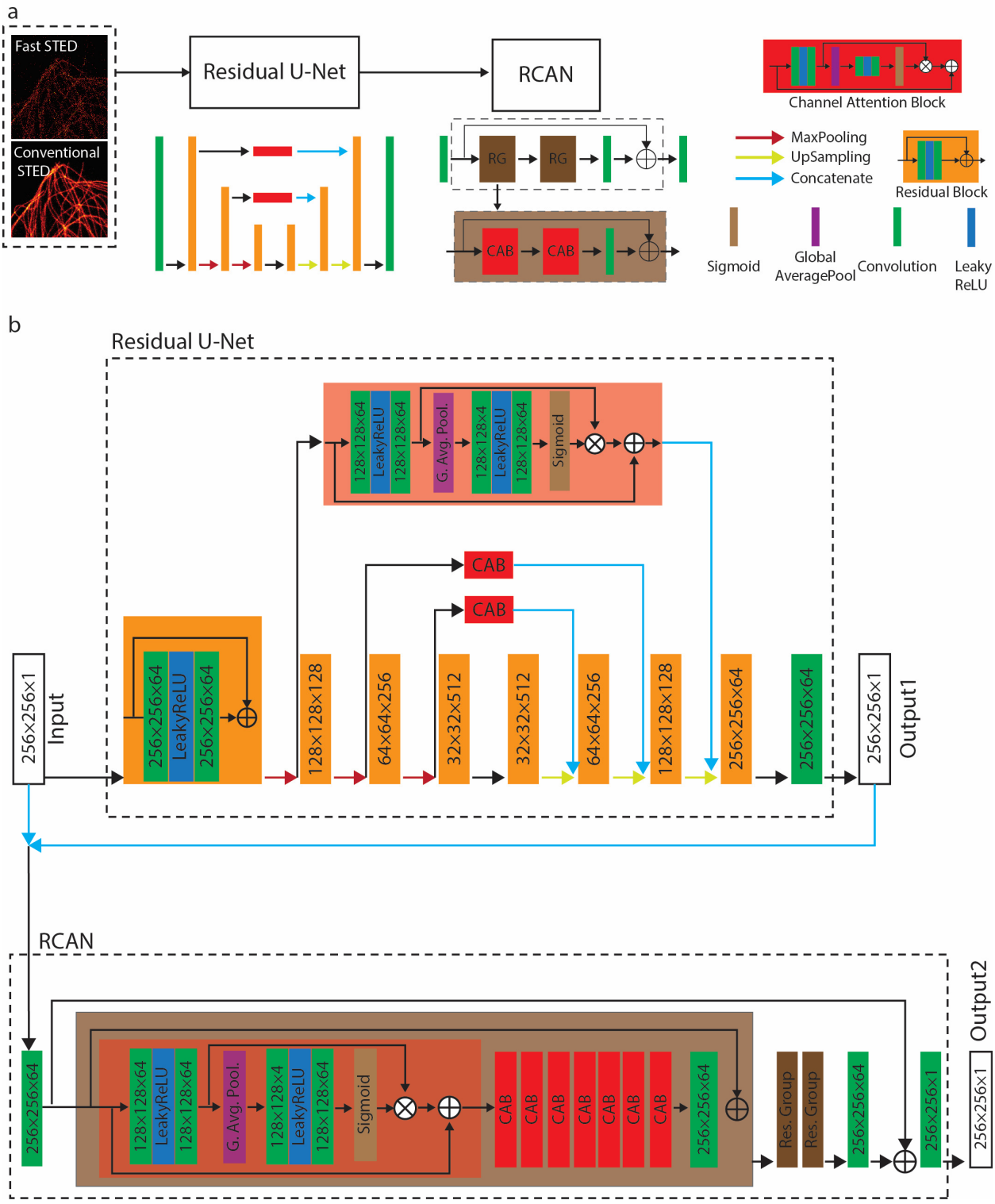
[6]Faculty of Physics and Astronomy, Institute of Applied Optics and Biophysics, Friedrich Schiller University Jena, Jena, Germany

[7]Jena School for Microbial Communication, Friedrich Schiller University Jena, Jena, Germany

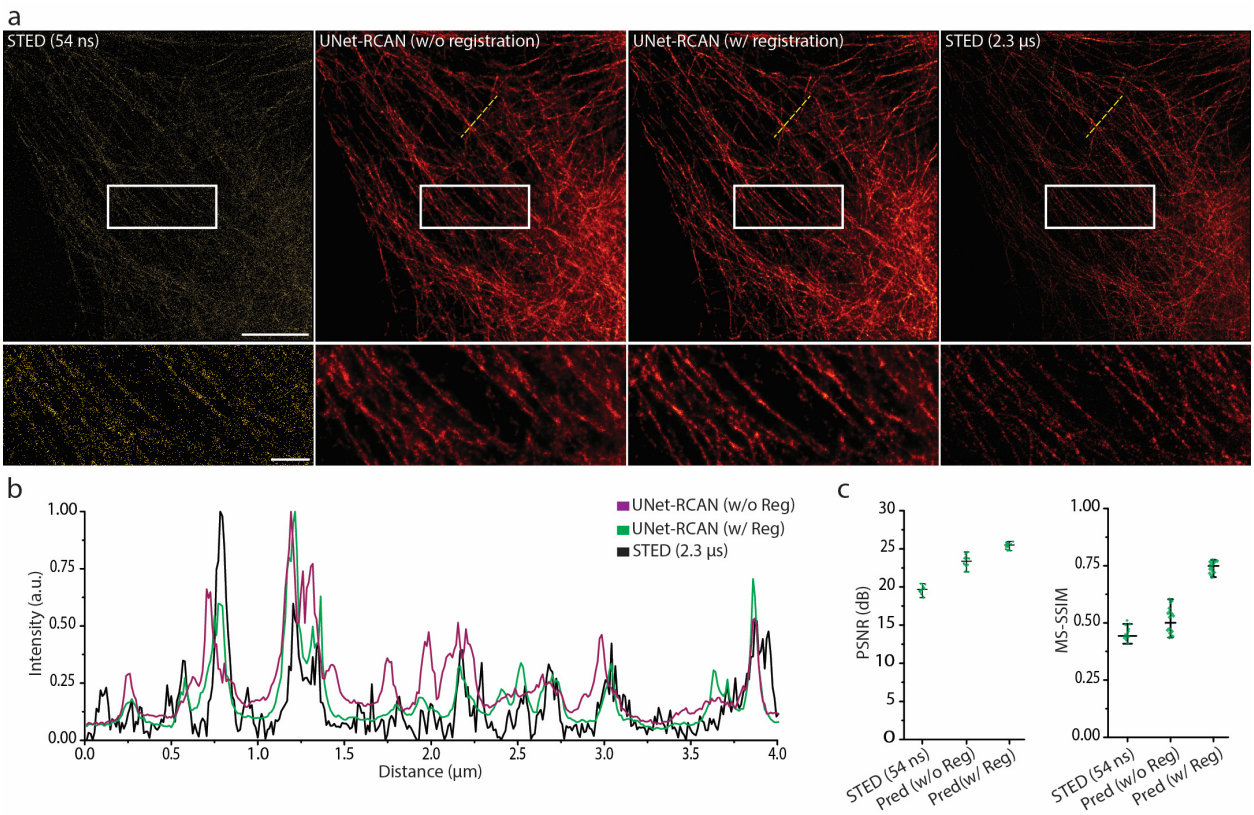
[8]Medical Research Council Human Immunology Unit, Weatherall Institute of Molecular Medicine, University of Oxford, Oxford, United Kingdom

[9]Translational Neuroinflammation and Automated Microscopy, Fraunhofer Institute for Translational Medicine and Pharmacology ITMP, Göttingen, Germany

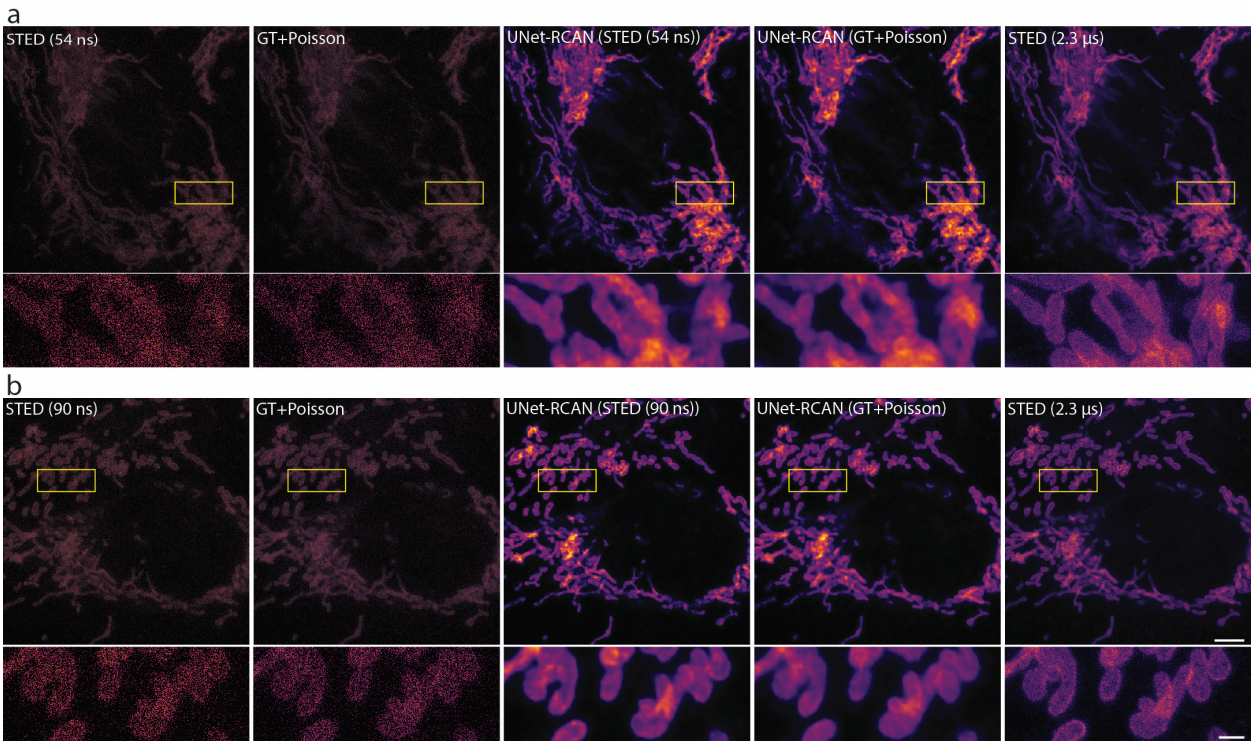
*Correspondence to Kyu Young Han: kyhan@creol.ucf.edu



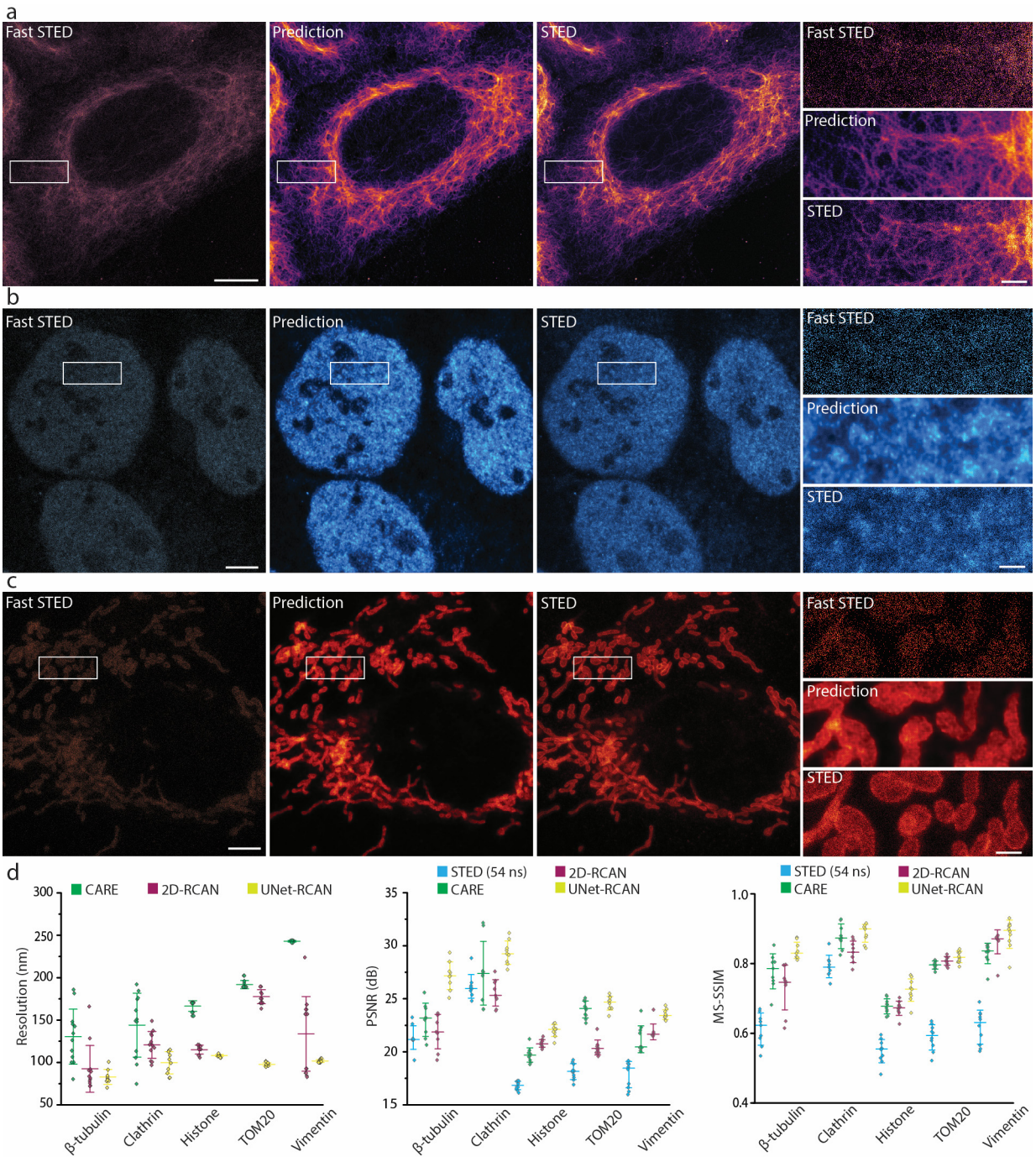
Supplementary Fig. 1, The architecture of UNet-RCAN for restoring fast STED imaging data. (a) The schematic of two-step prediction with UNet-RCAN. (b) Detailed architecture of UNet-RCAN. CAB, channel attention block; G. Avg. Pool., global average pooling; Res. Group, residual group. The model has one input and two outputs. Both output1 and output2 contribute to the loss function.



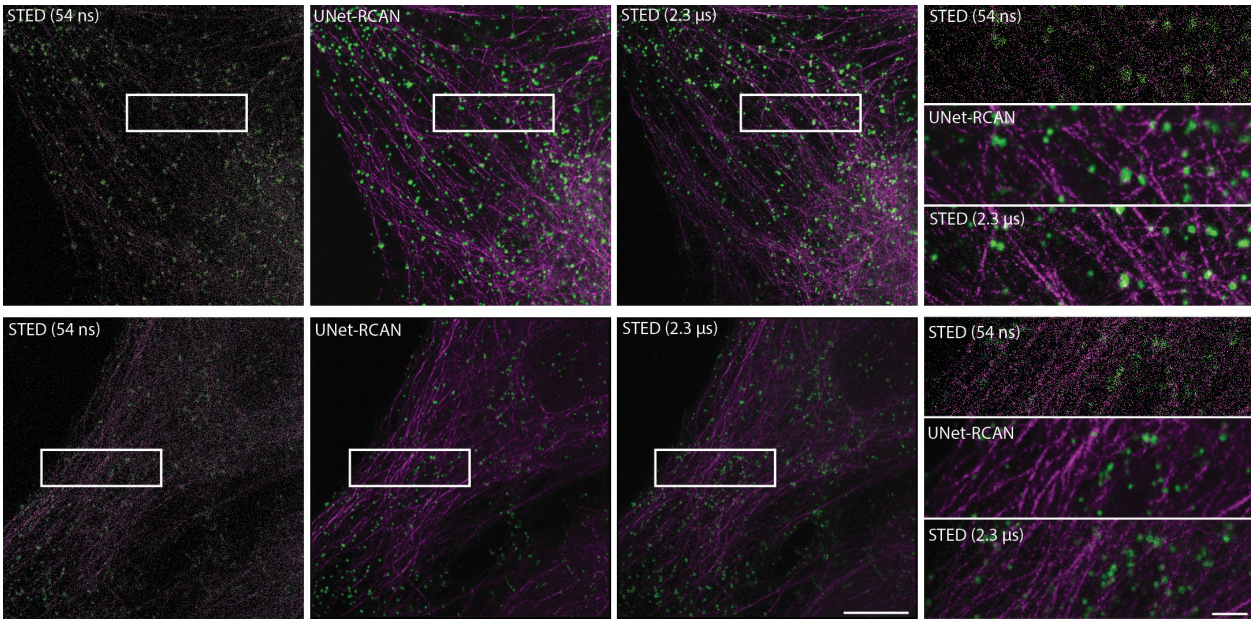
Supplementary Fig. 2, Registration of noisy input and ground-truth STED images. Registration improves prediction accuracy. Predicted STED images (a), line profiles (b), and quantitative assessment (c) by UNet-RCAN with and without registration of the noisy and ground-truth images by drift correction. Line profiles were measured along the yellow dashed lines. Scale bars, 5 µm and 1 µm (magnified regions).



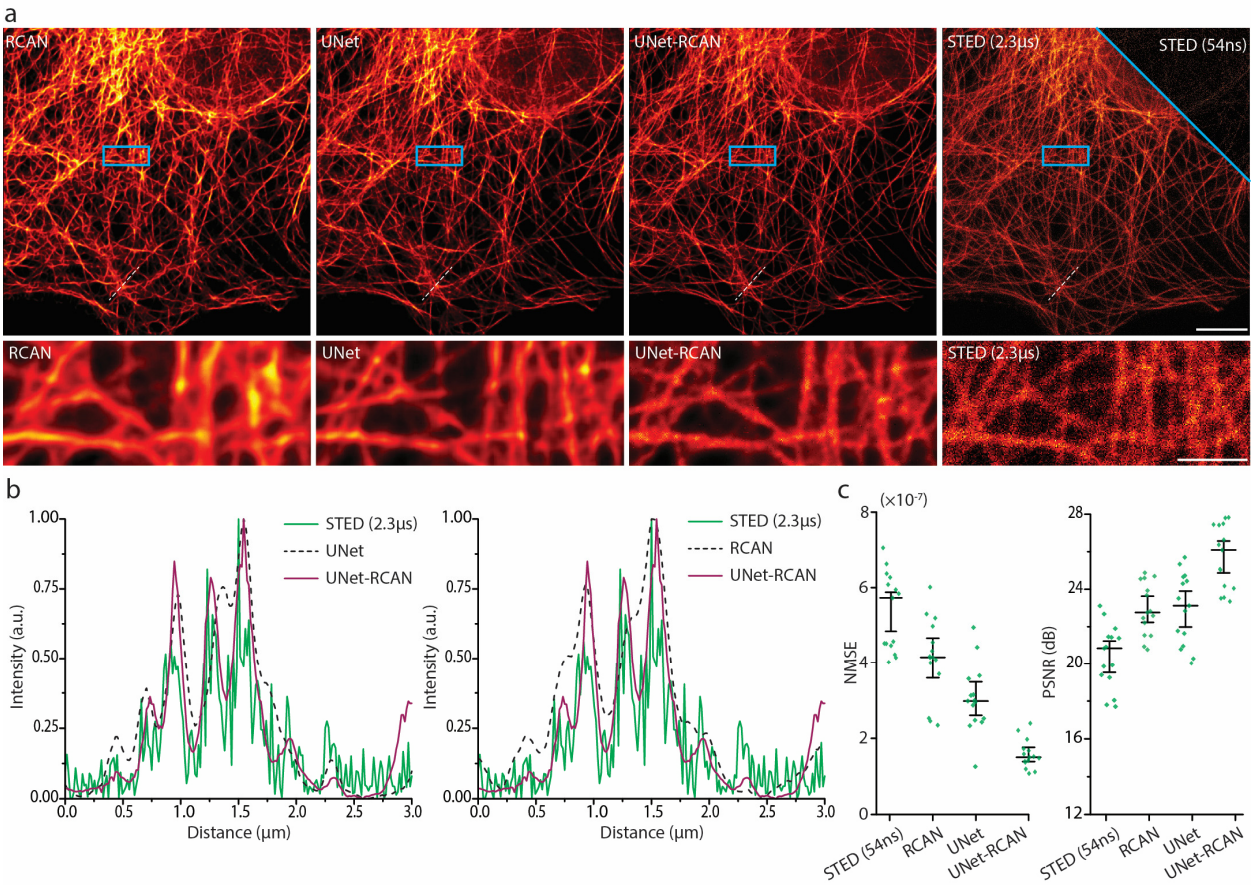
Supplementary Fig. 3, Comparison of semi-synthetic data and sequentially acquired noisy data. The predicted STED results from semi-synthetic data show similar results to those of well registered pairs of images. Different levels of SNR were tested, i.e., with a pixel time of 54 ns (a) or 90 ns (b) by adding Poisson noise to STED data with a pixel time of 2.3 µs. STED images of TOM20 labeled with Atto647N in U2OS cells. Scale bars, 5 µm and 1 µm (magnified regions).



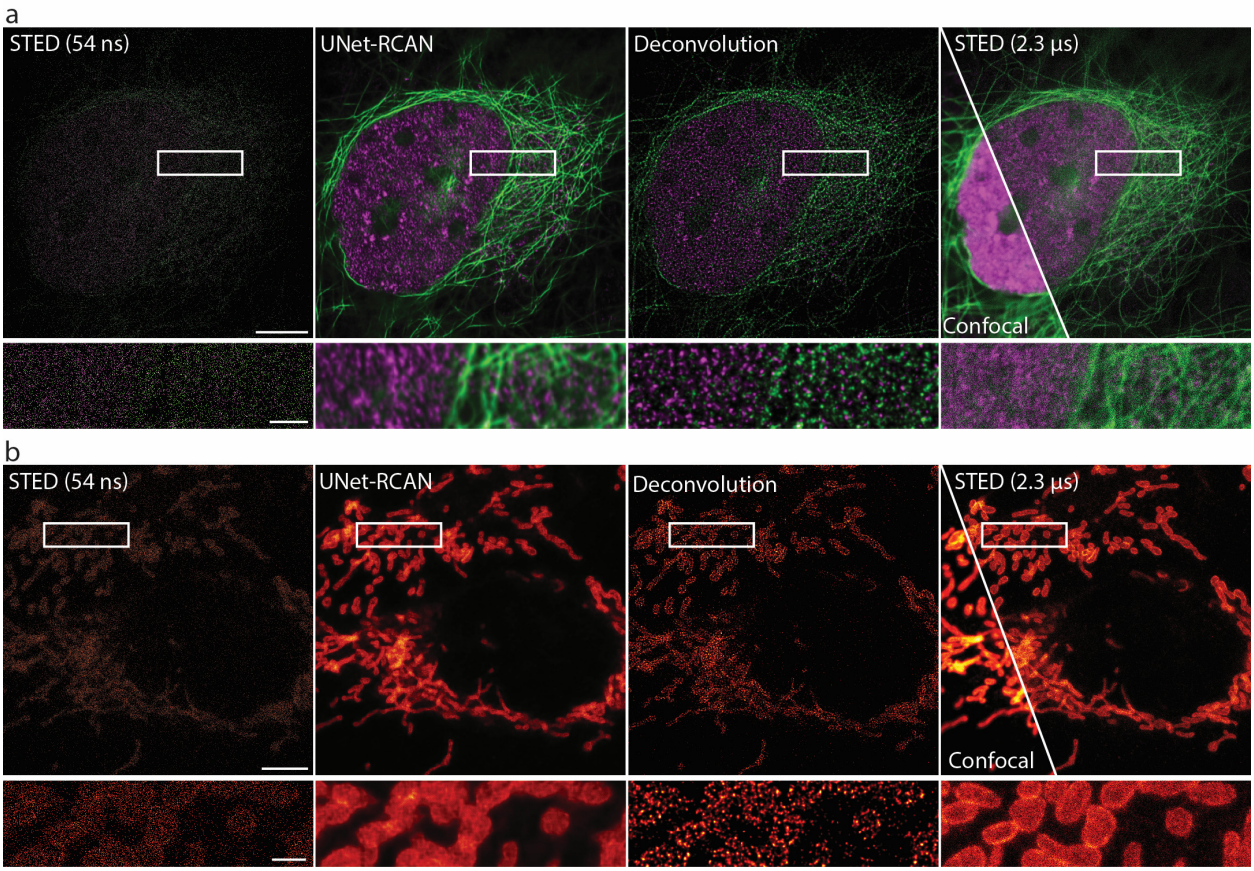
Supplementary Fig. 4, Image restoration results of 2D-STED images by UNet-RCAN on subcellular structures and comparison of the performances of UNet-RCAN, CARE, and 2D-RCAN. (a) Vimentin labeled with STAR635P, (b) Histone (H3K9ac) labeled with Atto647N, and (c) TOM20 labeled with Atto647N in fixed U2OS cells. Scale bars, 5 µm and 1 µm (magnified regions). (d) Five different markers were used for testing: β-tubulin (STAR635P), clathrin (STAR580), histone (Atto647N), TOM20 (Atto647N), and vimentin (STAR635P). PSNR and MS-SSIM were calculated with reference to ground-truth STED images (GT; Δt= 2.3 µs). The resolution was obtained by decorrelation analysis. Mean and standard deviation are displayed (n = 10).



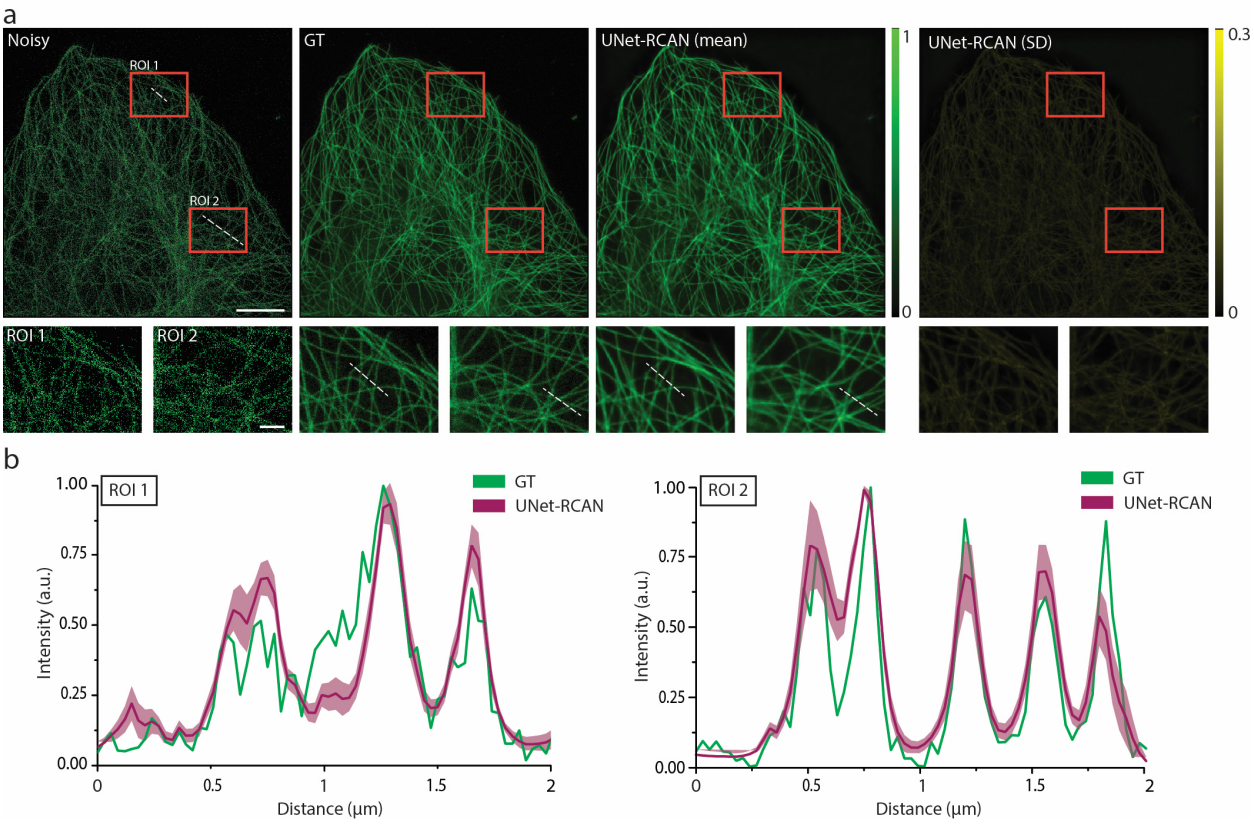
Supplementary Fig. 5, Restoring two-color fast STED imaging with UNet-RCAN. STED images of β-tubulin (STAR635P, magenta) and clathrin (STAR580, green) in U2OS cells with a pixel time of 54 ns. The ground-truth STED images were captured with a pixel time of 2.3 µs. Scale bar, 5 µm and 1 µm (magnified regions).



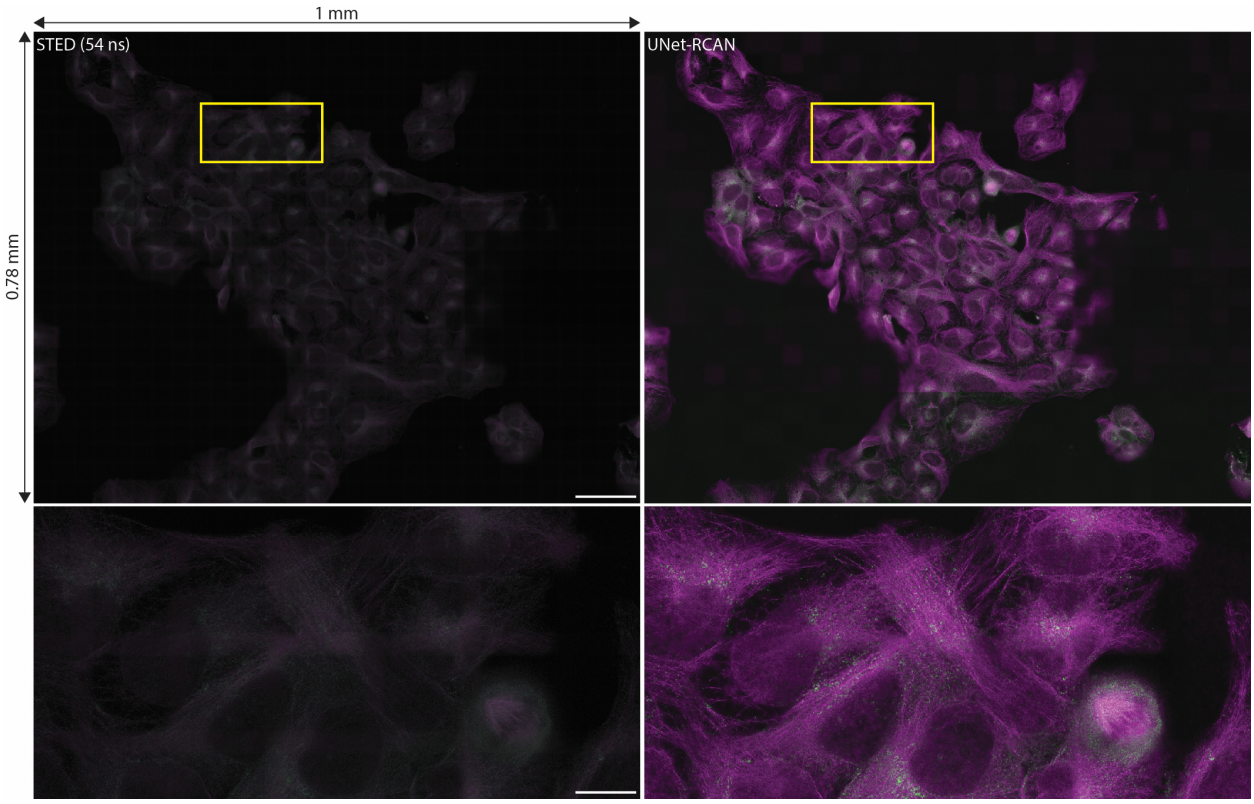
Supplementary Fig. 6, Comparison of the denoising performance of fast STED imaging with UNet-RCAN, residual U-Net, and 2D-RCAN. (a) β-tubulin labeled with STAR635P in fixed U2OS cells was imaged by a STED microscope with a dwell time of 54 ns (noisy input) and 2.3 µs (GT). The denoising is performed by UNet-RCAN, U-Net, and RCAN on the same noisy input. (b) Line profile measurements along the dashed line for GT and predictions by UNet-RCAN, U-Net, and RCAN. (c) Normalized mean squared error (NMSE) and PSNR of the predictions by UNet-RCAN, U-Net, and RCAN. The analysis shows the average and standard deviation for each parameter (n = 10). Scale bars, 5 µm and 1 µm for the magnified regions.



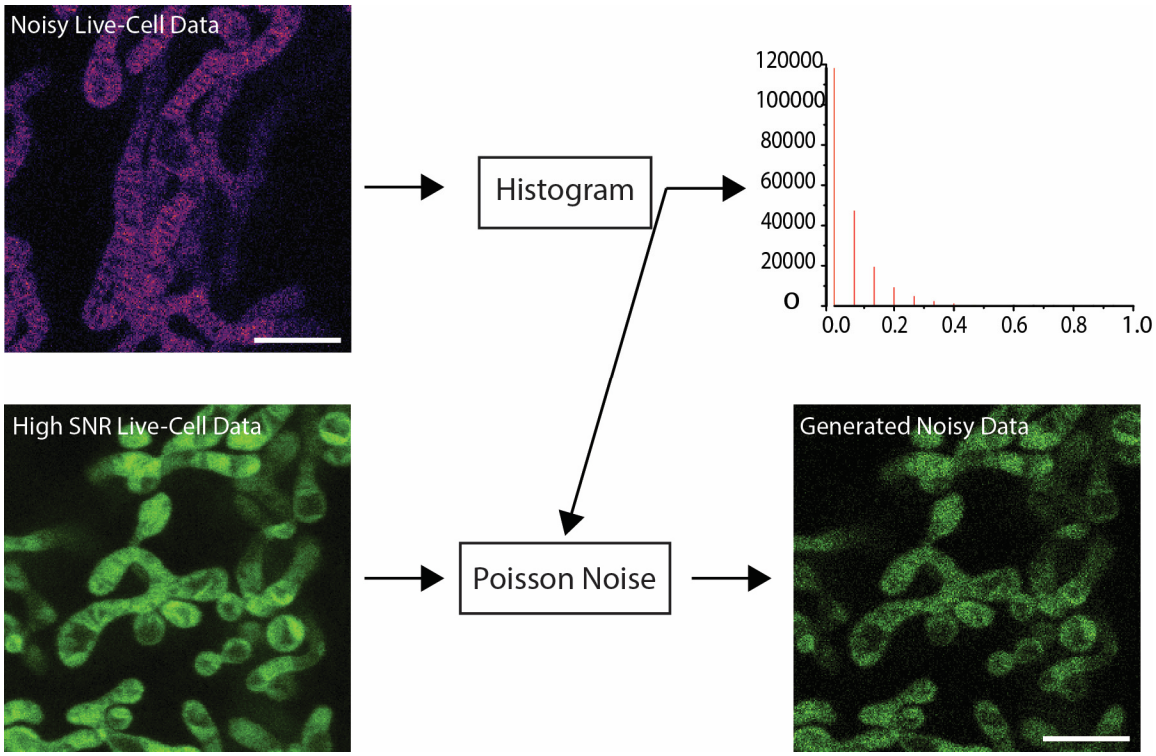
Supplementary Fig. 7, Comparison of denoising by UNet-RCAN and deconvolution. Denoising fast STED imaging of (a) β-tubulin (STAR580, green) and histone (Atto647N, magenta), and (b) TOM20 (Atto647N) in U2UOS cells. Separate denoising tasks were performed by UNet-RCAN and deconvolution on noisy STED data captured with a pixel time of 54 ns. Deconvolution was performed with Huygens software (See Methods). Scale bars, 5 µm and 1 µm (magnified regions).



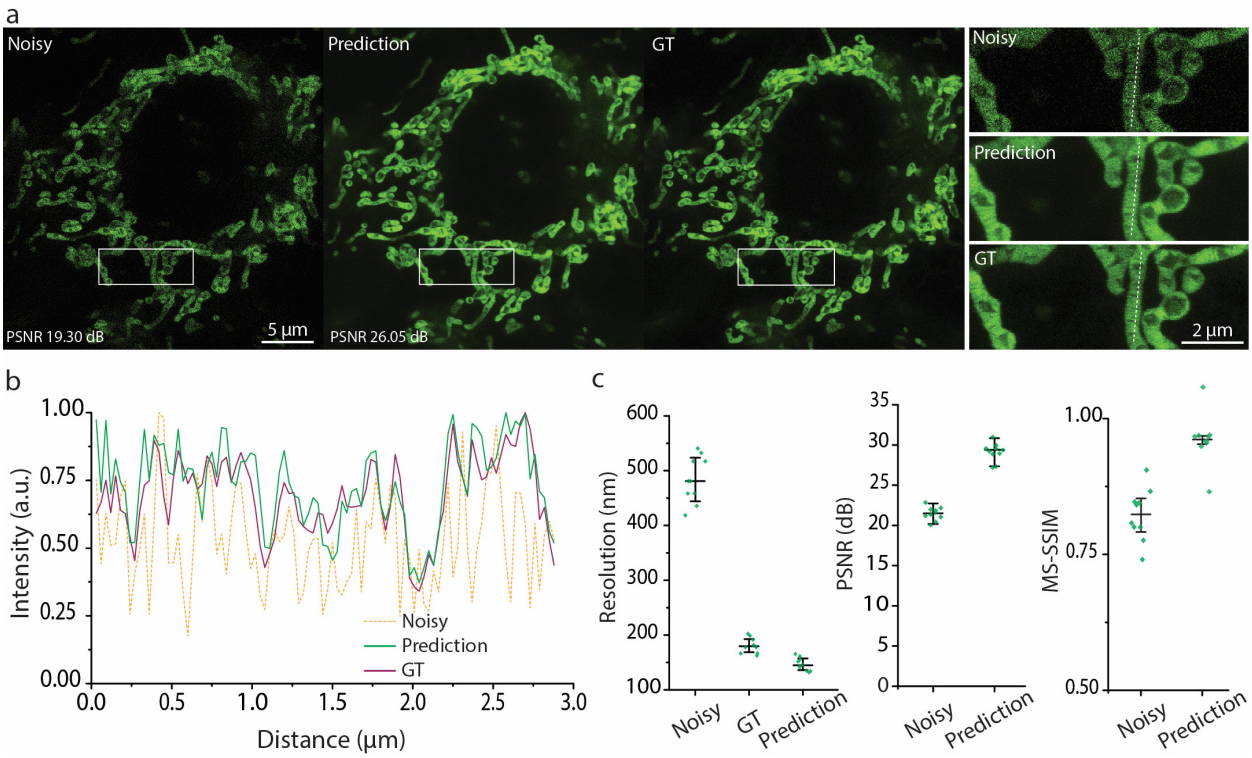
Supplementary Fig. 8, Prediction reliability by UNet-RCAN. (a) An ensemble is formed by training 10 UNet-RCAN networks to restore noisy STED microtubule data (STAR635P). An ensemble disagreement is measured by calculating the mean and standard deviation (SD) of the ensemble prediction results. (b) The mean and standard deviation of line profiles are measured in two regions (ROI 1 and ROI 2).



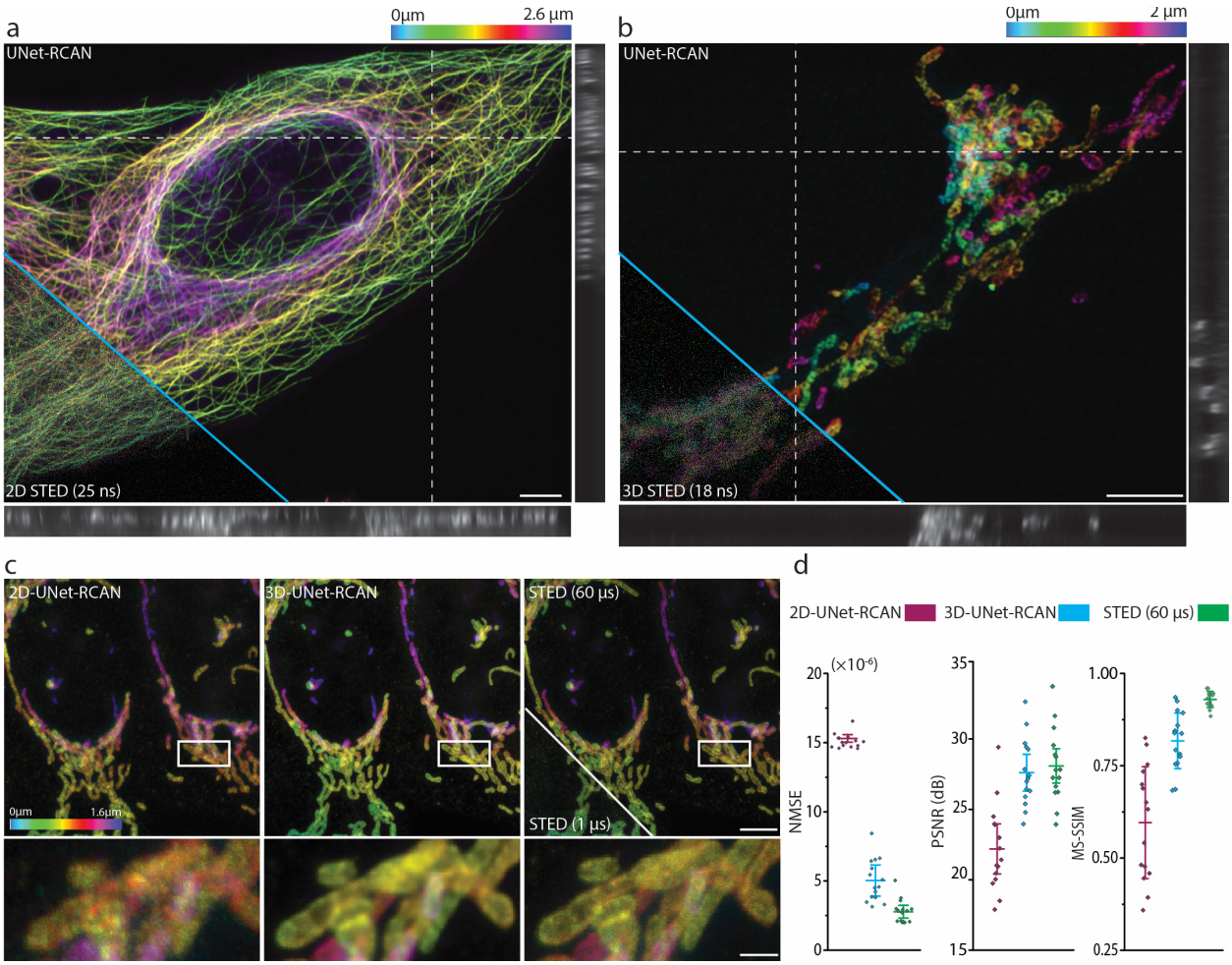
Supplementary Fig. 9, High-throughput STED imaging with UNet-RCAN. STED images of β-tubulin (STAR635P, magenta) and clathrin (STAR580, green) in U2OS cells with a pixel time of 54 ns. A grid of 31×24 images was denoised with UNet-RCAN and stitched together. Scale bars, 100 µm and 20 µm (magnified regions).



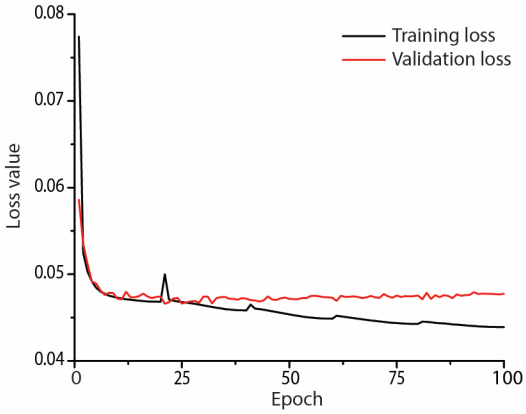
Supplementary Fig. 10, Semi-synthetic dataset generation. Poisson noise was applied to the high SNR STED images of cristae labeled with PK Mito Orange in HeLa cells to generate a pair of noisy and high SNR data for training UNet-RCAN. The amount of Poisson noise was adjusted such that the intensity histogram of the generated noisy data resembles that of the noisy live cell STED data (See Methods). Scale bars, 2μm.



Supplementary Fig. 11, Denoising performance of UNet-RCAN on the semi-synthetic dataset. (a) Denoising results of cristae labeled with PK Mito Orange in HeLa cells. The GT data was captured with a dwelling time of 90 µs. The noisy data was generated by adding Poisson noise. The prediction is the denoising result by UNet-RCAN. (b) Line profiles of noisy, prediction, and GT data along the dashed lines in (a). (c) Resolution analysis by decorrelation, PSNR, and MS-SSIM calculations were performed on the prediction results by UNet-RCAN. Mean and standard deviation are displayed (*n* = 10).



Supplementary Fig. 12, Prediction by 3D-UNet-RCAN on 2D and 3D STED imaging. 3D-UNet-RCAN prediction results for a noisy z-stack of (a) 2D-STED imaging of β-tubulin (STAR635P) and (b) 3D-STED imaging of TOM20 (Atto647N) in U2OS cells. The z pixel sizes are 170 nm and 65 nm, respectively. (c) Prediction results for a noisy z-stack of 3D STED imaging of TOM20 (Atto647N) by 2D- and 3D-UNet RCAN. The z pixel size is 40 nm. (d) NMSE, PSNR, and MS-SSIM analysis for prediction results by 2D- and 3D-UNet-RCAN (n=10). Scale bars, 5 μm and 1 μm for the magnified regions.



Supplementary Fig. 13, Training and validation loss curves for 2D-UNet-RCAN. The model was trained for denoising 2D STED imaging of microtubule (STAR635P) shown in Fig1. b.

Supplementary Note 1, Comparisons with other deep learning approaches

In cross-modality image restoration, a diffraction-limited confocal image is transformed into a super-resolved STED image with resolution enhancement by a deep convolutional neural network[1]. Different network architectures could perform this image transformation, such as generative adversarial networks (GAN)[2] or residual channel attention networks (RCAN)[3]. A transformation between confocal and STED imaging modalities at least requires a 3~5-fold resolution enhancement, i.e., from 250 nm to 50 nm; however, the cross-modality deep learning approaches have proven to be limited by a factor of 2-2.5 in terms of resolution enhancement[3]. Moreover, a lack of enough information often leads to exhibit artifacts.

Unlike the cross-modality image transformation, denoising is performed on noisy but super-resolved STED images to improve SNR. In denoising, the input data contains more information in terms of spatial resolution. This can help to reduce artifact generation and improve resolution enhancement. In Figs. 1f-h, we showed that denoising STED data clearly outperforms the cross-modality approach perceptually and according to the image quality assessment parameters.

Two popular network architectures suitable for denoising super-resolution data are UNet and RCAN. A UNet learns the features in an image dataset through convolutional layers and multiple down-sampling and up-sampling layers. Although the UNet effectively denoises diffraction-limited imaging data such as widefield images, its output does not reliably preserve high-frequency information. This is likely due to the fact that there is no mechanism to prioritize high-frequency information. Moreover, in UNet, a final image is reconstructed through downsampling and upsampling layers rather than applying the convolutional filters on the original noisy super-resolved data.

On the other hand, RCAN contains channel attention blocks and several skip connections, which help prioritize and maintain high-frequency information in super-resolution image reconstruction. Moreover, in RCAN, final super-resolved images are restored by applying filters on the original noisy data. This lowers the possibility of missing high-frequency information. However, our STED denoising results with RCAN show that although its final result is superior to UNet in terms of resolution, it generates more high-frequency artifacts, which may be due to its CAB building blocks, especially when the input SNR is extremely poor.

We showed that by combining UNet and RCAN, denoising could be effectively performed on fast STED data while we can maintain the super-resolution and prevent high-frequency artifact generation (Supplementary Fig. 6).

Supplementary Tables

Supplementary Table 1. Parameters and training time for CARE, 2D-RCAN, and UNet-RCAN.

	CARE	2D-RCAN	2D-UNet-RCAN	3D-UNet-RCAN
# Iterations per epoch	70	1,080	1,080	1080
Batch size	16	1	1	1
Patch size	256×256	256×256	256×256	160×160
Epochs	200	200	200	200
Number of parameters	3,790,850	3,944,073	16,684,270	152,935,406
Training time	1 h 17 m	11 h 40 m	8 h 10 m	30 h

Supplementary Table 2. Detailed computing hardware information.

Processor	AMD Ryzen 9 5900X 12-Core Processor 3.70 GHz
RAM	64 GB
GPU	NVIDIA GeForce RTX 3080 Ti

Supplementary Table 3. Performance comparison chart of UNet-RCAN, CARE, and 2D-RCAN in terms of SNR.

	Noisy	CARE	2D-RCAN	UNet-RCAN
β-tubulin	21.3±1.1 dB	23.0±1.6 dB	22.0±1.6 dB	27.2±1.3 dB
Clathrin	26.2±1.1 dB	27.4±3.0 dB	25.6±1.2 dB	29.3±1.1 dB
Histone	16.2±0.6 dB	20.4±0.8 dB	21.2±0.8 dB	21.6±0.9 dB
TOM20	18.0±0.7 dB	23.1±1.3 dB	20.9±0.8 dB	24.6±0.6 dB
Vimentin	17.7±0.9 dB	23.0±1.8 dB	23.0±1.1 dB	24.2±1.1 dB

Supplementary Table 4. Performance comparison chart of UNet-RCAN, CARE, and 2D-RCAN in terms of similarity.

	Noisy	CARE	2D-RCAN	UNet-RCAN
β-tubulin	0.61±0.04	0.77±0.05	0.73±0.06	0.83±0.02
Clathrin	0.79±0.03	0.87±0.03	0.83±0.03	0.88±0.02
Histone	0.53±0.06	0.67±0.04	0.66±0.04	0.70±0.06
TOM20	0.59±0.03	0.79±0.02	0.80±0.01	0.81±0.02
Vimentin	0.58±0.05	0.81±0.05	0.83±0.04	0.85±0.06

Supplementary Table 5. Performance comparison chart of UNet-RCAN, CARE, and 2D-RCAN in terms of resolution measured by decorrelation analysis.

	CARE	2D-RCAN	UNet-RCAN
β-tubulin	80±3 nm	71±3 nm	51±1 nm
Clathrin	122±5 nm	103±6 nm	81±4 nm
Histone	166±2 nm	115±2 nm	110±1 nm
TOM20	193±2 nm	179±3 nm	98±2 nm
Vimentin	243±1 nm	115±13 nm	101±1 nm

Supplementary Table 6. Acquisition settings of STED imaging.

Figures		
1b	Exc. power = 20% STED power = 50% Resonant scanning Gating: 0.4-12 ns Leica STED	Fluorophore: STAR635P, λ_{exc} = 635 nm, λ_{STED} = 775 nm Pixel time: 0.072 μs (noisy) and 2.3 μs (ground-truth)
3a SF 2a,4a,5,6a,7a, 9		Fluorophore: STAR635P, λ_{exc} = 635 nm, λ_{STED} = 775 nm Pixel time: 0.054 μs (noisy) and 2.3 μs (ground-truth)
3a		Fluorophore: Alexa 594, λ_{exc} = 594 nm, λ_{STED} = 775 nm Pixel time: 0.054 μs (noisy) and 2.3 μs (ground-truth)
SF 12a		Fluorophore: STAR635P, λ_{exc} = 635 nm, λ_{STED} = 775 nm Pixel time: 0.025 μs (noisy) and 1μs (ground-truth)
1f SF 3a, 4b, 4c, 7a, 7b		Fluorophore: Atto647N, λ_{exc} = 647 nm, λ_{STED} = 775 nm Pixel time: 0.054 μs (noisy) and 2.3 μs (ground-truth)
SF 3b		Fluorophore: Atto647N, λ_{exc} = 647 nm, λ_{STED} = 775 nm Pixel time: 0.090 μs (noisy) and 2.3 μs (ground-truth)
SF 5, 7a, 9		Fluorophore: STAR580, λ_{exc} = 580 nm, λ_{STED} = 775 nm Pixel time: 0.054 μs (noisy) and 2.3 μs (ground-truth)
2d, 2e		Fluorophore: Atto647N, λ_{exc} = 647 nm, λ_{STED} = 775 nm Pixel time: [0.018,0.036,0.072,0.108,0.144] μs (noisy) and 2.3 μs (ground-truth)
2d, 2e		Fluorophore: STAR580, λ_{exc} = 580 nm, λ_{STED} = 775 nm Pixel time: [0.018,0.036,0.072,0.108,0.144] μs (noisy) and 2.3 μs (ground-truth)
2a	Exc. power = 20% STED power = [0%,10%,20%,50%,70%], Resonant scanning Gating: 0.4-12 ns Leica STED	Fluorophore: STAR635P, λ_{exc} = 635 nm, λ_{STED} = 775 nm Pixel time: 0.050 μs (noisy) and 1.0 μs (ground-truth)
3g SF 10b, 12b	Exc. power = 20% 2D-STED power = 50% z-STED power = 50% Resonant scanning	Fluorophore: Atto647N, λ_{exc} = 635 nm. λ_{STED} = 775 nm Pixel time: 0.018 μs (noisy) and 2.3 μs (ground-truth)

	Gating: 0.4-12 ns Leica STED	
SM 1	Exc. power = 4.5% STED power = 22% Galvo scanning Gating: 0.75-8 ns Abberior STED	Fluorophore: PK Mito Orange, λ_{exc} = 561 nm, λ_{STED} = 775 nm Pixel time: 30 μs, Line accumulation: 3
3c, 3d SF 11a SM 2, 3, 4	Exc. power = 4.5% STED power = 22% Galvo scanning Gating: 0.75-8 ns Abberior STED	Fluorophore: PK Mito Orange, λ_{exc} = 561 nm, λ_{STED} = 775 nm Pixel time: 1 μs (noisy)
SM 3	Exc. power = 1% STED power = 25% Galvo scanning Gating: 0.75-8 ns Abberior STED	Fluorophore: 647-SiR-CA, λ_{exc} = 640 nm, λ_{STED} = 775 nm Pixel time: 1 μs (noisy)
SF 12c	Exc. power = 5% 2D-STED power = 50% z-STED power = 50% Galvo scanning Gating: 0.4-12 ns Abberior STED	Fluorophore: Atto647N, λ_{exc} = 635 nm. λ_{STED} = 775 nm Pixel time: 1 μs (noisy) and 60 μs (ground-truth)
3h, SM 5	Exc. power = 35% 2D-STED power = 0% z-STED power = 100% Galvo scanning Gating: 0 ns Abberior STED	Fluorophore: NR4A , λ_{exc} = 561 nm, λ_{STED} = 775 nm Pixel time: 2 μs (noisy) and 20 μs (ground-truth)

Supplementary Table 7. Immunolabeling conditions.

Figures	Primary antibody	Secondary antibody	Fluorophore
1b, 2a, 3a SI 2a, 5, 6a,8a, 9,12a	Monoclonal Anti-β-Tubulin antibody produced in mouse, Sigma-Aldrich, T5293	Fab Fragment Goat Anti-Mouse IgG1, Jackson ImmunoResearch, 115-007-185	Abberior STAR 635P
2d, 2e SI 7a,	Monoclonal Anti-β-Tubulin antibody produced in mouse, Sigma-Aldrich, T5293	Fab Fragment Goat Anti-Mouse IgG1, Jackson ImmunoResearch, 115-007-185	Abberior STAR 580

SI 5, 9	Anti-Clathrin heavy chain antibody (ab21679)	Fab Fragment Goat Anti-Rabbit IgG, Jackson ImmunoResearch, 111-007-008	Abberior STAR 580
1f,2d,2e SI 4b, 7a	Anti-acetyl-Histone H3 (Lys9) in rabbit, Sigma-Aldrich, 07-352	Rabbit IgG (H&L) Antibody ATTO 647N Conjugated Pre-Adsorbed, ROCKLAND, 611-156-122	Atto 647N
3a	Anti-acetyl-Histone H3 (Lys9) in rabbit, Sigma-Aldrich, 07-352	Alexa Fluor® 594 AffiniPure $F(ab')_2$ Fragment Goat Anti-Rabbit IgG (H+L)	Alexa Fluor 594
3g SI 3a, 3b, 4c,7b, 12b,12c	Anti-TOMM20 antibody - Mitochondrial Marker, abcam, ab78547	Rabbit IgG (H&L) Antibody ATTO 647N Conjugated Pre-Adsorbed, ROCKLAND, 611-156-122	Atto 647N
SI 4a	Anti-Vimentin antibody, Mouse monoclonal (V6389-200UL)	Fab Fragment Goat Anti-Mouse IgG1, Jackson ImmunoResearch, 115-007-185	Abberior STAR 635P

References

1. Wang, H.D. et al. Deep learning enables cross-modality super-resolution in fluorescence microscopy. *Nat Methods* **16**, 103-110 (2019).
2. Ouyang, W., Aristov, A., Lelek, M., Hao, X. & Zimmer, C. Deep learning massively accelerates super-resolution localization microscopy. *Nat Biotechnol* **36**, 460-468 (2018).
3. Chen, J.J. et al. Three-dimensional residual channel attention networks denoise and sharpen fluorescence microscopy image volumes. *Nat Methods* **18**, 678-687 (2021).

Description of Additional Supplementary Files

File name: Supplementary Data 1
Description: The source data behind the graphs in the paper

File name: Supplementary Video 1
Description: Time-lapse STED imaging of mitochondria dynamics with a pixel time of 90 µs. HeLa cells were labeled with PK Mito Orange.

File name: Supplementary Video 2
Description: Fast deep-learning STED imaging of mitochondria dynamics with a pixel time of 1 µs. HeLa cells were labeled with PK Mito Orange.

File name: Supplementary Video 3
Description: Two-color live-cell deep-learning STED imaging of mitochondria (green) and ER (magenta) in HeLa cells with a pixel time of 1 µs. Mitochondria was labeled with PK Mito Orange, and ER was labeled with SiR-Halo.

File name: Supplementary Video 4
Description: Deep-learning live-cell STED imaging with deconvolution. COS-7 cells were labeled with PK Mito Orange.

File name: Supplementary Video 5
Description: Denoising fast 3D STED xz imaging of giant unilamellar vesicles (GUV) labeled with NR4A with a pixel time of 2 µs

nature portfolio

Corresponding author(s): Kyu Young Han

Last updated by author(s): Jun 10, 2023

Reporting Summary

Nature Portfolio wishes to improve the reproducibility of the work that we publish. This form provides structure for consistency and transparency in reporting. For further information on Nature Portfolio policies, see our Editorial Policies and the Editorial Policy Checklist.

Statistics

For all statistical analyses, confirm that the following items are present in the figure legend, table legend, main text, or Methods section.

n/a	Confirmed	
☐	☒	The exact sample size (*n*) for each experimental group/condition, given as a discrete number and unit of measurement
☐	☒	A statement on whether measurements were taken from distinct samples or whether the same sample was measured repeatedly
☒	☐	The statistical test(s) used AND whether they are one- or two-sided *Only common tests should be described solely by name; describe more complex techniques in the Methods section.*
☒	☐	A description of all covariates tested
☒	☐	A description of any assumptions or corrections, such as tests of normality and adjustment for multiple comparisons
☐	☒	A full description of the statistical parameters including central tendency (e.g. means) or other basic estimates (e.g. regression coefficient) AND variation (e.g. standard deviation) or associated estimates of uncertainty (e.g. confidence intervals)
☒	☐	For null hypothesis testing, the test statistic (e.g. *F*, *t*, *r*) with confidence intervals, effect sizes, degrees of freedom and *P* value noted *Give P values as exact values whenever suitable.*
☒	☐	For Bayesian analysis, information on the choice of priors and Markov chain Monte Carlo settings
☒	☐	For hierarchical and complex designs, identification of the appropriate level for tests and full reporting of outcomes
☒	☐	Estimates of effect sizes (e.g. Cohen's *d*, Pearson's *r*), indicating how they were calculated

Our web collection on statistics for biologists contains articles on many of the points above.

Software and code

Policy information about availability of computer code

Data collection	For image denoising on fixed samples, the images were collected by Leica SP8 3X STED. For denoising on live cell samples, the images were collected by Abberior STED Expert Line.
Data analysis	UNet-RCAN was used for denoising and cross-modality image transformation. The code is available from GitHub (https://github.com/vebrahimi1990/UNet_RCAN_Denoising.git). Resolution calculation by image decorrelation analysis was performed by ImageJ (ImageDecorrelationAnalysis_plugin). Deconvolution was performed by Huygens Essential (22.04).

For manuscripts utilizing custom algorithms or software that are central to the research but not yet described in published literature, software must be made available to editors and reviewers. We strongly encourage code deposition in a community repository (e.g. GitHub). See the Nature Portfolio guidelines for submitting code & software for further information.

Data

Policy information about availability of data

All manuscripts must include a data availability statement. This statement should provide the following information, where applicable:

- Accession codes, unique identifiers, or web links for publicly available datasets
- A description of any restrictions on data availability
- For clinical datasets or third party data, please ensure that the statement adheres to our policy

Data may be obtained from the authors upon reasonable request.

Human research participants

Policy information about studies involving human research participants and Sex and Gender in Research.

Reporting on sex and gender	n/a
Population characteristics	n/a
Recruitment	n/a
Ethics oversight	n/a

Note that full information on the approval of the study protocol must also be provided in the manuscript.

Field-specific reporting

Please select the one below that is the best fit for your research. If you are not sure, read the appropriate sections before making your selection.

☒ Life sciences ☐ Behavioural & social sciences ☐ Ecological, evolutionary & environmental sciences

For a reference copy of the document with all sections, see nature.com/documents/nr-reporting-summary-flat.pdf

Life sciences study design

All studies must disclose on these points even when the disclosure is negative.

Sample size	The exact sample size can be found in the Main Text and Supplementary Information.
Data exclusions	For training the model, we excluded the patches that did not contain sufficient amount of information. The details can be found in Method section (Preparation of training dataset). For testing, no data was excluded.
Replication	All the codes, data, and protocols are available for replicating the results of our experiments. All the STED denoising models were tested on at least 10 different testing data. The denoising results were quantified by averaging at least 10 different testing data.
Randomization	No allocation in experimental groups were performed.
Blinding	All the deep learning models were blindly tested with the data that was not used for training.

Reporting for specific materials, systems and methods

We require information from authors about some types of materials, experimental systems and methods used in many studies. Here, indicate whether each material, system or method listed is relevant to your study. If you are not sure if a list item applies to your research, read the appropriate section before selecting a response.

Materials & experimental systems

n/a	Involved in the study
☐	☒ Antibodies
☐	☒ Eukaryotic cell lines
☒	☐ Palaeontology and archaeology
☒	☐ Animals and other organisms
☒	☐ Clinical data
☒	☐ Dual use research of concern

Methods

n/a	Involved in the study
☒	☐ ChIP-seq
☒	☐ Flow cytometry
☒	☐ MRI-based neuroimaging

Antibodies

Antibodies used

mouse anti-β-tubulin, Sigma-Aldrich (T5293), anti-clathrin heavy chain (ab21679), rabbit anti-acetyl-histone H3 (Lys9), Sigma-Aldrich (07-352), anti-TOMM20 antibody - mitochondrial marker, abcam (ab78547), mouse anti-vimentin antibody, (V6389-200UL), fab goat anti-mouse IgG1, Jackson ImmunoResearch (115-007-185), fab goat anti-rabbit IgG, Jackson ImmunoResearch (111-007-008), rabbit IgG (H&L) ATTO 647N conjugated pre-adsorbed, ROCKLAND (611-156-122), alexa fluor 594 AffiniPure F(ab')$_2$ goat anti-rabbit IgG (H+L).

Validation

All the antibodies have been extensively used in previous studies. We compared the staining patterns with images in other literatures.

Eukaryotic cell lines

Policy information about cell lines and Sex and Gender in Research

Cell line source(s)

The following cell lines were used:
U2OS (ATCC), HeLa, COS-7

Authentication

The used cell lines were not authenticated.

Mycoplasma contamination

Cell lines were not tested for mycoplasma contamination. However, we often examined DAPI images to check potential contamination.

Commonly misidentified lines
(See ICLAC register)

The used cell lines were not commonly misidentified.